Comparative Analysis of CFD and PIV Base Buffeting Data Considering Decomposition Techniques and Filtering Effects in the Measurement Chain

By T. Horchler, P. Blinde†, C. Serhan‡, K. Hannemann¶ AND F. Schrijer†
Deutsches Zentrum für Luft- und Raumfahrt DLR, Spacecraft Department,
Bunsenstr. 10, 37073 Göttingen

Significant dynamical loads on the nozzle structure of launch vehicles during ascent can cause deformations and eventually complete failure of rocket engines. This effect, known as base buffeting, has been observed for the Ariane V vehicle and is caused by a strong flow seperation at the base of the main body and subsequent reattachement on the nozzle. In order to investigate this phenomenon and to assess mitigation strategies, wind tunnel experiments and numerical simulations of a subscale wind tunnel model at transonic flight conditions have been conducted.

This work compares an experimental and numerical dataset of a launch vehicle tail flow field in terms of Proper Orthogonal Decomposition (POD) and Dynamic Mode Decomposition (DMD). Both methods allow to isolate dominant flow features and, in case of DMD, to determine an oscillation frequency associated with the mode.

In order to account for the different spatial and temporal resolutions of the datasets, the numerical simulation data is subsampled and spatially filtered to match the experimental Particle Image Velocimetry (PIV) dataset as closely as possible. This approach also allows to assess the effect of spatio-temporal filtering on the CFD mode structure. Additionally, POD and DMD modes of the numerical surface pressure distribution are compared to high-resolution experimental surface pressure measurements.

1. Introduction

During the ascent of the Ariane 5 launch vehicle significant dynamic loads on the nozzle can cause deformations which may lead to catastrophic failure of the engine. This phenomenon is known as base buffeting and is caused by a strong flow separation at the base of the launcher vehicle. Wind tunnel experiments and CFD investigations have been conducted to gain more insight into this phenomenon, to improve modeling and to assess mitigation strategies (see, e.g., [4, 11]). Compared to experiments, CFD computations typically achieve a much higher spatial and temporal resolution but span a shorter time period and may not capture all flow features correctly. In experiments on the other hand, it is easy to achieve long time series but high sampling frequencies are difficult to realize. Furthermore, the experimental measurement chain introduces spatial

† Delft Technical University
‡ Deutsches Zentrum für Luft- und Raumfahrt DLR, Spacecraft Department, Braunschweig
¶ Deutsches Zentrum für Luft- und Raumfahrt DLR, Spacecraft Department, Göttingen

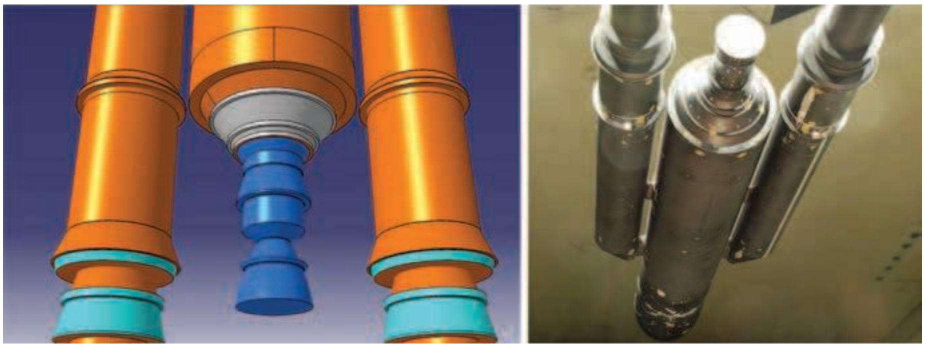

FIGURE 1. Left: CAD description of the geometry used in the IDDES. Right: picture of the model used for the PIV experiment mounted in the DNW HST wind tunnel (source [6])

and temporal filtering (modulation) that damps any frequencies above a certain threshold and leaves all flow scales smaller than a certain size unresolved. Given these merits and drawbacks of both types of investigations, comparing the outcome of experiments and simulations is essential for the proper interpretation and mutual validation of their results.

Experimental and CFD results are often only compared in terms of mean and fluctuating surface pressure data and velocity fields. Meanwhile, methods for data decomposition like proper orthogonal decomposition (POD) [1, 9] and dynamic mode decomposition (DMD) [10, 15] have shown potential in analyzing experimental and numerical results. Both methods isolate dominant flow modes which could be used to construct low-order models of the flow. The methods rely on the availability of suitable input data only and do not require making any assumptions about the flow. POD [1, 7, 9] is a well established analysis tool in the fluid dynamics community. Using snapshots with spatially resolved data, it yields spatial modes on an orthogonal basis ranked by energy content. DMD [10, 15] emerged as a new tool only around 2008 and has since been applied successfully to many academic and industrial problems [3, 8, 10, 12, 13, 17]. Using time resolved data sampled at a constant frequency, DMD provides single-frequency modes ranked by amplitude.

The present work investigates the suitability of using POD and DMD to compare experimental and numerical results. The study compares two datasets of the flow over the nozzle of the Ariane 5, one obtained via experiments and one via a simulation. The experimental data consists of unsteady pressure measurements in conjunction with time-resolved planar PIV measurements. These results were obtained in the framework of the ESA TRP ‘Unsteady Subscale Force Measurements Within a Launch Vehicle Base Buffeting Environment’ [4, 6, 11]. The CFD data was obtained by an improved delayed detached-eddy simulation (IDDES) using DLR TAU code [16] in the follow-up ESA TRP ‘Launcher Base Flows and Shock Interaction Regions Improved Load Characterization’ .

2. Description of the Experimental and Numerical Datasets

The present study uses a subset of the results from pressure measurements described by [4], PIV experiments described by [11] and a revised version of the improved delayed detached eddy simulation (IDDES) described by [6]. For detailed descriptions of the experimental and numerical investigations, the reader is referred to those studies.

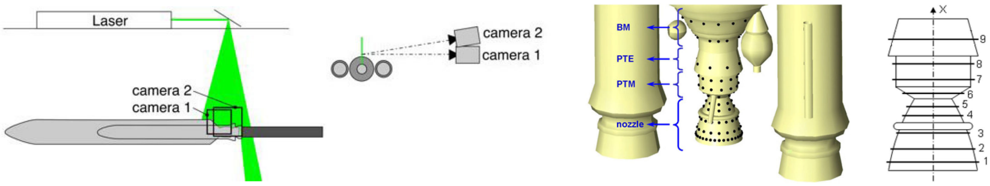

(a) PIV setup (b) Locations of the pressure sensors.

FIGURE 2. Experimental setups. Left: PIV setup (adapted from [11]). Right: Location of pressure sensors (source: [4])

All datasets represent a Mach 0.8 flow over a 1:60 scale model of the Ariane 5 launcher with two booster held without supporting struts near the base (see Fig. 1). This configuration is referred to as "attaches midi" in [4, 11] and configuration 1 in [6]. The diameter of the model main body is D=0.0908 m. Experiments were performed in the DNW High Speed Wind Tunnel with the following freestream conditions which were also used for the simulation [4, 6]: static freestream pressure p_∞ = 65740 Pa, freestream velocity V_∞ = 266.1 ms^{-1}, freestream dynamic pressure q_∞ = 29.4 Pa and the unit Reynolds number Re_m = 12.8 10^6 m^{-1}.

Fig. 2 shows the experimental setup used to obtain the PIV results as well as the location of the field of view [11]. The size of the field of view was 110 x 100 mm. The vector pitch is 0.72 mm obtained using a final interrogation window size of 32 x 32 pixels and 75 percent overlap. Image pairs were recorded at a frequency of 2.7 kHz corresponding to a Strouhal number St_D = 0.9. The dataset consists of 2728 snapshots giving a total sample length of 1010 ms.

Pressure measurements were obtained in a separate experimental campaign using 144 flush mounted cylindrical differential unsteady pressure transducers located in eight rings distributed over the nozzle [4] (see Fig. 2). Measurements were obtained at a sampling rate of 12.8 kHz. The dataset consists of 131076 samples for each transducer resulting in a total sample length of 10.24 s.

The IDDES was performed using the DLR TAU code [16] on an hybrid grid with 23 million points (Fig. 3). In the present case, the Spalart-Allmaras (SA) turbulence model was used in combination with a low-dissipation central differencing scheme. The RANS/LES switching is based on a characteristic grid length scale which is chosen to be proportional to the largest local cell dimension. The simulation results consist of three velocity components, pressure, density, viscosity, vorticity and the Q-value. The physical timestep in the original simulation is 2 microseconds.

For the present study the dataset was downsampled to 9631 snapshots with a time separation of 20 microseconds corresponding to a frequency of 50 kHz and a Strouhal number of St_D = 17.1. The resulting dataset spans a duration of 0.193 s. To further reduce the data volume, a quasi two-dimensional plane was extracted consisting of 97268 grid points.

Table 1 provides an overview of the PIV and simulation properties used for the present study.

In order to compare the experimental and the numerical datasets, the 2D CFD data has been extracted at the same location as the PIV data. Additionally, the CFD sampling rate has artificially been reduced to match the sampling rate of the PIV experiments. This dataset will be referred to as the raw CFD dataset in Sec. 4. The CFD has been further processed to reproduce the PIV reconstruction process. In a first step, the field of view

Property	PIV data	Exp. surface pressure	CFD data
Sampling frequency (kHz)	2.7 (St_D= 0.9)	12.7 (St_D = 4.3)	10 (St_D = 3.3)
Number of samples	2,728	131,076	1,635
Duration (ms)	1010	10240	163.5
Number of gridpoints	13,984	144	60,080

TABLE 1. Properties of datasets

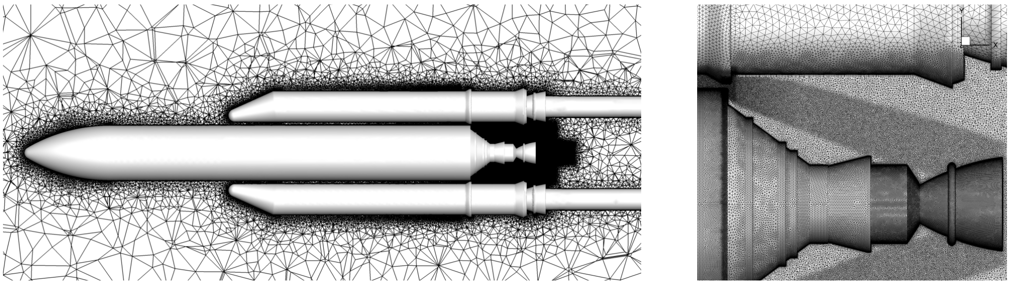

FIGURE 3. CFD grid setup. Left: 2D slice of the full domain. Right: zoom of nozzle region.

has been reduced to the PIV field of view which excludes the model near wall region because reflections from the model surface prevent accurate PIV measurements. The data has also been interpolated from the CFD grid to the coarser PIV grid. In a second step the velocity field has been averaged over a window size of 2.88 $\times$ 2.88 mm giving a vector pitch of 0.72 mm and an overlap of 75%. This dataset will be referred to as the filtered CFD data.

3. Data Decomposition Techniques

Typical realistic flows incorporate a wealth of structures with different spatial and temporal scales that interact in complex ways. Flow measurements and simulations aim to obtain accurate representations of the true flowfield. As these techniques improve over time, they lead to large amounts of data with increasingly resolved complex flow features. Isolating the particular flow features of interest for a certain analysis can be a challenging task that may be assisted by a variety of post-processing techniques. These include techniques that rely on flow modeling assumption, statistical techniques such as conditional averaging, and data decomposition such as POD and DMD which are the topic of the present study. As mentioned in the introduction, both POD and DMD isolate dominant flow modes and can be used to construct low-order models of the flow. In general, there are different ways in which a dataset (and therefore flow field) can be decomposed. A particular unique decomposition is obtained by imposing restrictions on the resulting decomposition. POD and DMD differ in the way that they impose these restrictions. POD imposes restrictions on the spatial structure of the data to obtain spatial modes on an orthogonal basis while DMD imposes restrictions on its temporal structure to achieve single-frequency modes. Due to the nature of the respective decomposition, POD requires spatially resolved input data and DMD requires time resolved input data. Another important consequence of the way the decompositions are defined is that the POD modes are not necessarily coherent in time and the DMD modes are not necessarily coherent in space. Furthermore, it is noted that neither POD nor DMD make any assumptions about the flow and that as a consequence, the resulting modes do not necessarily represent physical phenomena. A very useful property of the implementations of POD and DMD is that the algorithms can be setup to only return the first specified number of modes, thereby significantly reducing computation time, and the resulting modes are ranked in terms of energy content (for POD) and mode amplitude (for DMD). It should however be noted that energy and/or amplitude are not in all cases the most relevant measures to rank flow structures.

3.1. *Proper Orthogonal Decomposition*

POD is a well established analysis tool in the fluid dynamics community [1,7,9]. In order to apply POD, the data is rearranged in a snapshot matrix Ψ_0 in which each column represents the spatial data at one instant of time (the name Ψ_0 which is unusual in the context of POD is chosen here to mirror the description of DMD in the next section). The POD of the snapshot matrix Ψ_0 can be shown to be identical to its single value decomposition (SVD) (see e.g. [10])

$$\Psi_0 = U \Sigma V^* \tag{3.1}$$

where U is an orthonormal matrix containing the left singular vectors that represent the POD modes; Σ is a pseudo-diagonal and semi-positive definite matrix with diagonal entries containing the singular values that represent the amplitudes of the POD modes, and V is an orthonormal matrix containing the right singular vectors that represent the time evolution.

3.2. *Dynamic Mode Decomposition*

Dynamic mode decomposition was originally proposed in [10] and has since been modified [5,15]. This work uses an extended version [5] of the original algorithm that enforces a sparse reconstruction of the full flowfield by an optimized choice of modes.

In order to apply DMD to any type of dataset, the data must be sampled at a constant frequency and is then rearranged in two snapshot matrices

$$\Psi_0 = [\psi_0 \;\; \psi_1 \;\; \dots \;\; \psi_{N-1}] \tag{3.2}$$

$$\Psi_1 = [\psi_1 \;\; \psi_2 \;\; \dots \;\; \psi_N] \tag{3.3}$$

where each column $\{\psi_0, \dots, \psi_N\}$ represents the spatial data at one instant of time. The method assumes a linear and time-invariant mapping A between the snapshots

$$\Psi_1 = A \Psi_0 \tag{3.4}$$

The goal is now to find a low-order representation of A in terms of the DMD modes of Ψ_0. To do this, the data matrix Ψ_0 is first decomposed using singular value decomposition as a means of preconditioning (note the similarity to POD up until this step)

$$\Psi_0 = U \Sigma V^*. \tag{3.5}$$

A DMD representation of A is then given by

$$F_{\mathrm{DMD}} = U^* \Psi_1 V \Sigma^{-1} \tag{3.6}$$

whose properties are sought in terms of a eigenvalue decomposition. Using the eigenvalues and eigenvectors, the data is then decomposed in

$$\underbrace{\begin{bmatrix}\psi_0 & \dots & \psi_{N-1}\end{bmatrix}}_{\Psi_0} \approx \underbrace{\begin{bmatrix}\Phi_0 & \dots & \Phi_{N-1}\end{bmatrix}}_{\Phi} \underbrace{\begin{bmatrix}\alpha_1 & & \\ & \ddots & \\ & & \alpha_r\end{bmatrix}}_{D_\alpha} \underbrace{\begin{bmatrix}1 & \mu_1 & \dots & \mu_1^{N-1} \\ \vdots & \vdots & \ddots & \vdots \\ 1 & \mu_r & \dots & \mu_r^{N-1}\end{bmatrix}}_{V_{\text{and}}} \tag{3.7}$$

where Φ_i are the DMD modes, D_α is a diagonal matrix containing an amplitude and V_{and} contains the temporal evolution. In [5] it is shown that the calculation of the amplitudes α_i can be formulated as an optimization problem

$$\underset{\alpha}{\text{minimize}} \;\; J(\alpha) = \left\| \Sigma V^* - Y D_\alpha V_{\text{and}} \right\|^2 . \tag{3.8}$$

This algorithm is then extended to enforce a sparse solution by adding a term that punishes reconstructions based on many modes.

$$\underset{\alpha}{\text{minimize}} \;\; J(\alpha) + \gamma \sum_{i=1}^{r} |\alpha_i| \tag{3.9}$$

where γ is a user defined number that determines the level of sparsity. The quality of approximation is described by a performance loss parameter (in percent) defined by

$$P_{\text{loss}} := 100 \sqrt{\frac{J(\alpha)}{J(0)}} = 100 \frac{\left\| \Psi_0 - \Phi D_\alpha V_{\text{and}} \right\|}{\left\| \Psi_0 \right\|} . \tag{3.10}$$

4. Results

4.1. *Mean Flow Field*

Fig. 4 compares the mean flow fields obtained via PIV (left column) and CFD (middle column). In addition, the right column shows the impact of spatially filtering the CFD data to mimic the resolution of PIV as described in Sec. 2. The top row shows the velocity in x-direction and the bottom row the velocity in z-direction. The PIV data (left column) does not follow the exact nozzle contour because no reliable velocity measurements could be obtained close to the wall due to poor seeding and lighting conditions in that region. The depicted region for the CFD data (middle column) was chosen to correspond to the overall PIV field of view but with the near wall region included. For the filtered CFD data (right column) this region was excluded to better resemble the PIV results.

In general terms, the CFD and PIV data yield the same average flow fields. A shear layer emanates from the edge of the main body. It grows in size in downstream direction as a result of the typical thickening behavior of mixing layers and the unsteady flapping behaviour of the shear layer. This flapping could also be observed when comparing different instantaneous snapshots. Below the shear layer exists a low speed region. Within this region, the simulation data shows a small layer with reversed flow over the surface of the model (see top middle figure). Small pockets with stronger reversed flow can be observed directly downstream of small steps and corners in the nozzle geometry. The average flowfield obtained by PIV (top left figure) shows virtually no reversed flow. It should however be noted that no measurements are available in a small layer directly above the surface and where reversed flow is likely to occur. In comparison, also the filtered CFD results (top right figure) does not show any reversed flow. Further compar-

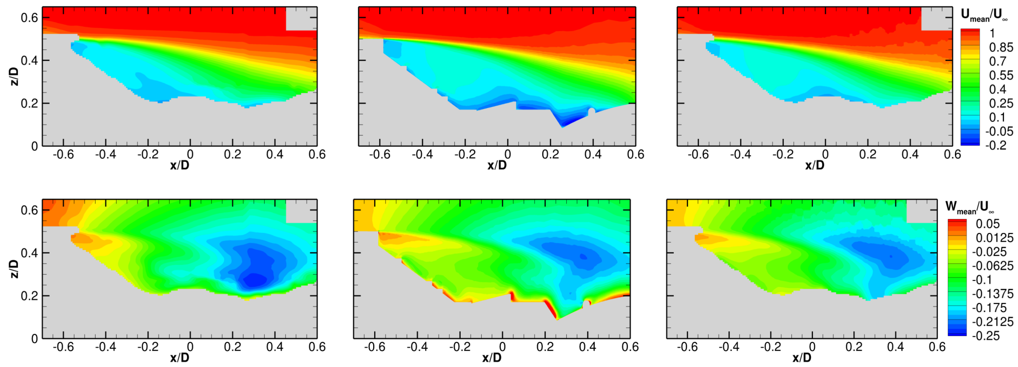

(a) PIV (b) CFD (c) Filtered CFD

FIGURE 4. Comparison of the mean velocity fields. Left: PIV data. Centre: raw CFD data. Right: filtered CFD data. Top row: Streamwise velocity u. Bottom row: Wall normal velocity w.

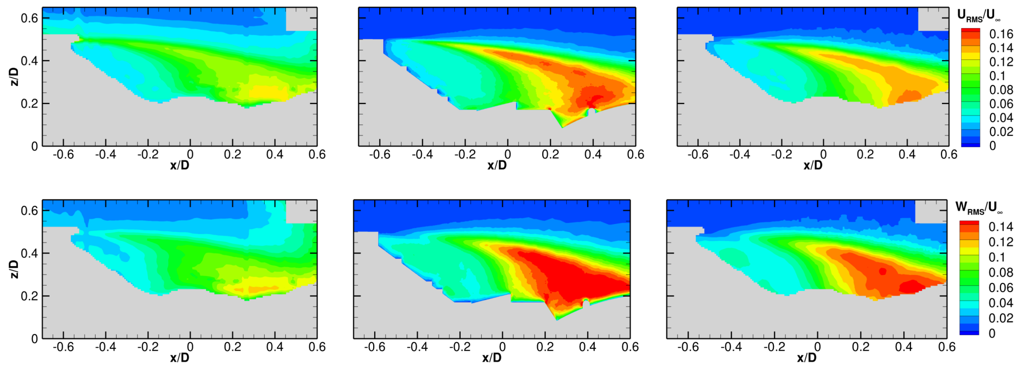

(a) PIV (b) CFD (c) Filtered CFD

FIGURE 5. Comparison of the rms velocity fluctuations. Left: PIV data. Centre: raw CFD data. Right: filtered CFD data. Top row: Streamwise velocity u. Bottom row: Wall normal velocity w.

ison of the two flow fields shows subtle differences in the the mean shape and size of the shear layer and the low-speed region below.

The comparison of the wall-normal (z) velocity component shows a number of differences between the experimental and the numerical data. The region with maximum z-velocity lies closer to the surface and is larger than in the simulation data. Also, a pocket of higher z-velocity extends further towards the launch vehicle base. No significant difference is observed between the filtered and unfiltered CFD data.

4.2. *RMS Velocity*

Fig. 5 compares the RMS of the velocity fluctuations. The figure shows that whereas the PIV and CFD data qualitatively lead to the same flow field, there is a large difference in the strengths of the fluctuations. The CFD data shows considerably stronger fluctuations (see middle and right column) compared to the PIV data. Even when the CFD data is filtered in a similar manner as the experimental data, there still remains a difference of about 4 % of the free-stream velocity compared to the PIV data. These observations apply to the x- as well as the z-velocity component.

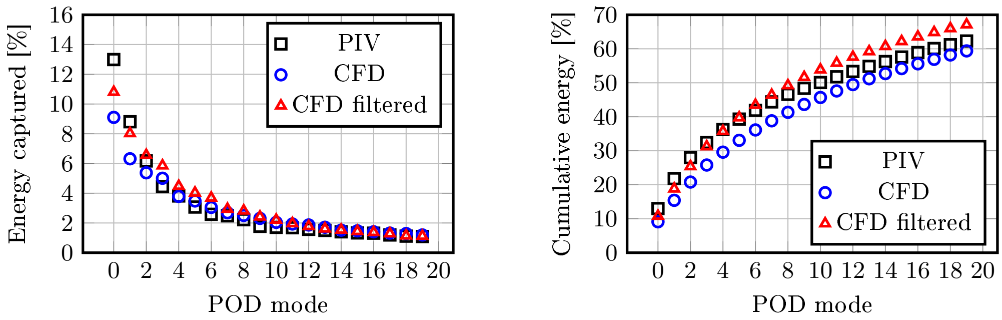

(a) POD mode energy content.

(b) Cumulative POD mode energy.

FIGURE 6. Single mode and cumulative relative energy content of the POD modes.

4.3. *POD of Velocity Data*

In this section, the POD modes of the experimental and numerical datasets are compared. Even though the POD has been applied to both velocity components simultaneously, the x velocity will only be reported here for brevity. Generally, all observations are also valid for the wall normal velocity.

Fig. 6 compares the energy spectrum of the velocity POD modes. Consistent with the theoretical framework, the modes are ranked in terms of energy content, where the first mode contains the largest amount of energy. Comparison between the PIV and CFD modes shows that the first CFD mode contains less relative energy and the decay towards higher modes is less pronounced. Since these plots represent the relative energy content per mode, this means that the total energy is more evenly distributed across the modes for the CFD results. This indicates that there is a larger range of length scales present in the flow that needs to be represented by larger number of modes. This also becomes clear when the energy spectrum for the filtered CFD data is observed, here the relative energy is shifted towards the lower modes which are more pronounced compared to the raw CFD data.

Fig. 7 shows the first six POD mode shapes of the streamwise velocity fluctuations ranked by energy content. Generally, the PIV and the filtered CFD mode shapes agree qualitatively very well for all modes shown even though there are small differences in position and mode amplitude. The variation in the amplitudes can be directly linked to the different distributions of energy (compare Fig. 6) and the different total content of energy, represented by the RMS values in Sec. 4.1.

Since differences in between the absolute POD mode amplitude of PIV and CFD are caused by a combination of various effects, it is of little interest to compare them directly.

When comparing the raw CFD modes with the PIV and filtered CFD results, one notices that modes 0,1 and 4 agree quite well in shape and position but modes 2,3 and 5 differ. Especially mode 2 and 3 look fundamentally different than PIV or the filtered CFD modes. In order to identify if this difference is caused by the PIV field of view or the filtering process, the raw CFD data has been decomposed into POD modes considering only the PIV field of view (see Fig. 8). One notices that the overall mode shapes are identical and that therefore the chosen field of view has a large impact on the POD mode structure. Since the overall field of view is similar for the raw CFD and the PIV data, the difference is likely to be caused by the near wall region which is not considered for PIV

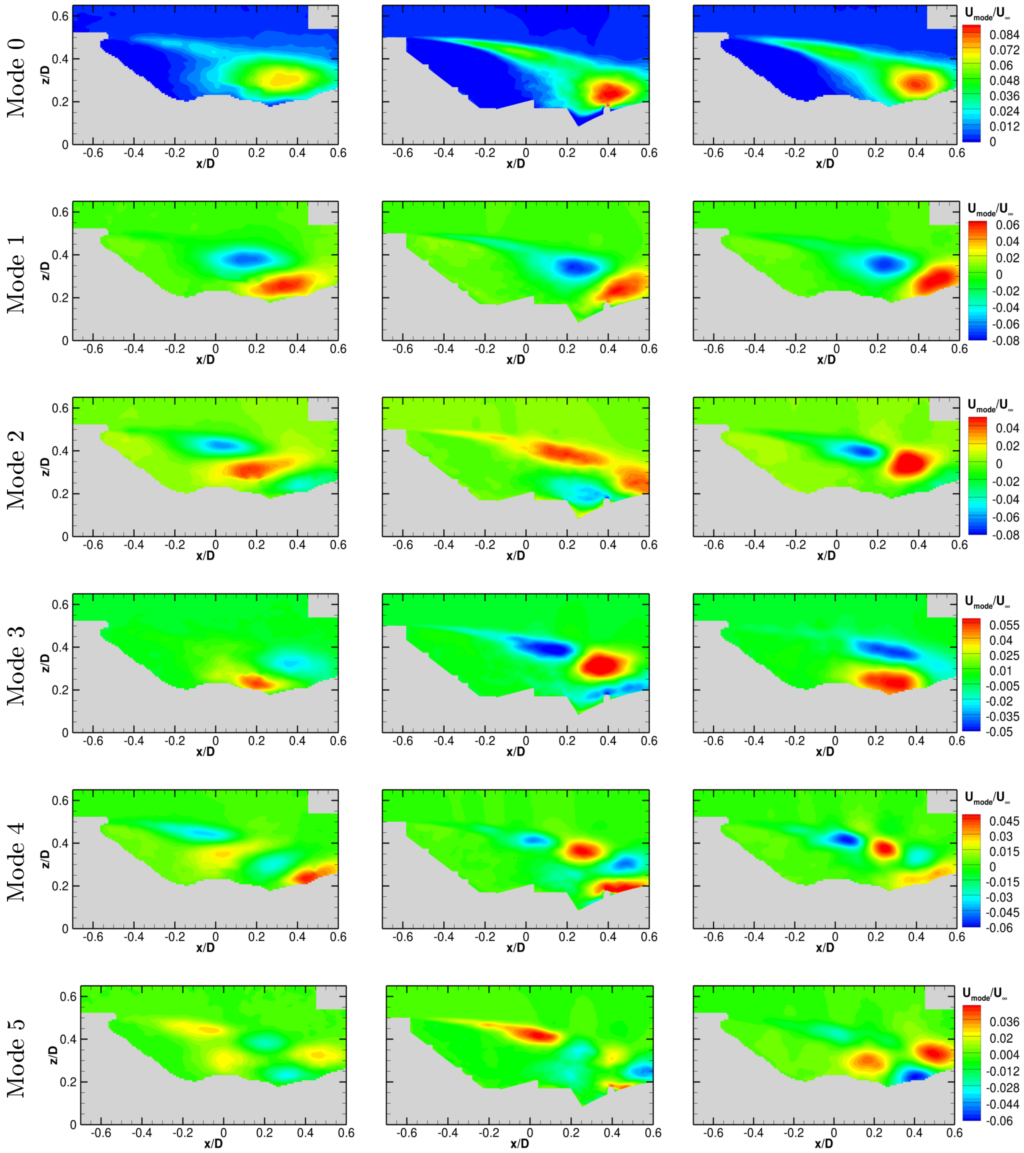

(a) PIV (b) CFD (c) Filtered CFD

FIGURE 7. The first 6 POD modes of the streamwise velocity fluctuations.

and the filtered data. Indeed, mode 3 for example shows a region of reversed flow near the nozzle surface which lies outside the PIV field of view.

An interpretation of the first modes was given in [11]. Mode 0 represents a single patch of high velocity fluid whose action is to either fill up or empty the separated region. This can be interpreted as a shear layer flapping motion which shifts the reattachement point on the nozzle. Mode 1 shows two regions of opposite velocity direction that undulate the shear layer. In the same sense, mode 2 is a higher order undulation with two zero

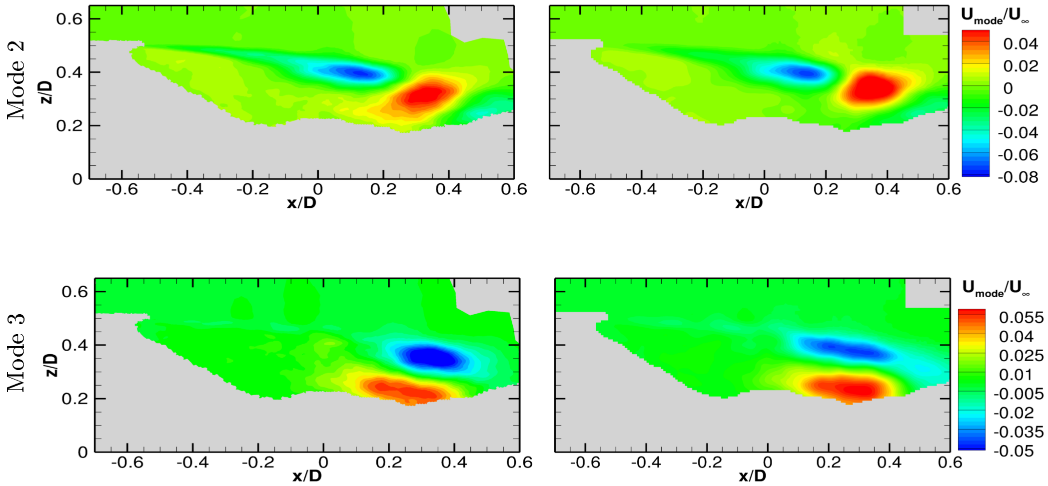

(a) CFD with PIV field of view (b) Filtered CFD

FIGURE 8. The effect of the PIV field of view on the CFD mode shapes.

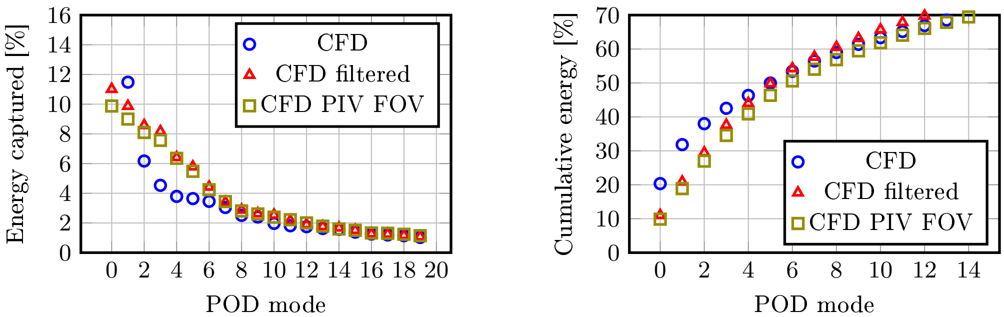

(a) Pressure POD mode energy content. (b) Cumulative pressure POD mode energy.

FIGURE 9. Single mode and cumulative energy content of the pressure POD modes.

nodes between the alternating velocity regions, which allows in combination with mode 1 a convecting motion of the undulation.

4.4. *POD of Pressure Data*

Even though there is no experimental pressure field data available, it is interesting to decompose the CFD pressure in terms of POD modes: the nozzle wall pressure generates the forces that cause base buffeting and secondly, the 2D modes can be compared to the POD of the surface pressure distribution measured by the Kulite transducers.

Fig. 9 shows the distribution of relative energy over the different pressure modes . There is a large difference between the filtered and unfiltered CFD data for the first modes (see Fig. 9(a)). For the unfiltered CFD data, the first mode contains more relative energy than the filtered CFD. However, the relative energy drop to the next modes is more pronounced while for the filtered CFD mode the energy decay is more gradual.

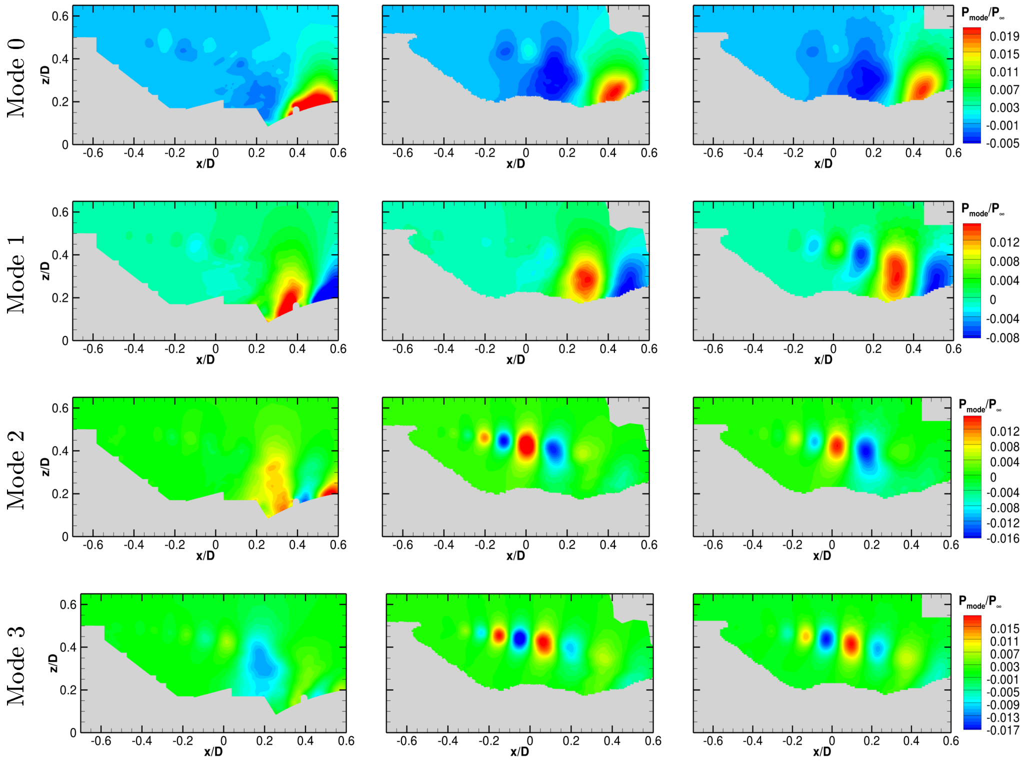

(a) CFD (b) CFD with PIV field of view (c) Filtered CFD

FIGURE 10. Pressure POD modes.

The qualitative shape of the zeroth mode is similar for the filtered and raw CFD data while for the raw data, the mode is very strong near the wall.

Mode 1 still compares qualitatively well while all higher mode shapes look different. Starting from mode 1, one notices the onset of vortical structures in the shear layer that impinge on the nozzle. In the raw CFD data, this mode is dominated by the foot print of this shear layer mode which is only barely visible in the current plotting scale. The same shear layer mode appears clearer in the filtered CFD results.

Modes 2 and 3 differ greatly for the raw and filtered CFD results. While the filtered results clearly show a shear layer mode, the raw CFD data only give strong fluctuations near the wall for mode 2 while mode 3 doesn't show any coherent shape. The differences are again caused by the different field of views. The middle column of Fig. 10 shows the CFD POD modes when the PIV field of view is considered. As for the velocity POD modes, these modes are again similar to the filtered CFD results showing that the field of view has a profound influence on the resulting POD modes. Mode 2 also suggests that the near wall region is especially important since for the raw CFD this mode is almost completely located outside the PIV field of view.

Fig. 11 shows the mode shapes of the first two CFD c_p modes on the Ariane 5 nozzle. Both modes show a similar structure on the front (at $270°$) and back (at $90°$) with two distinct regions of opposite sign. They differ however in their relative orientation: for

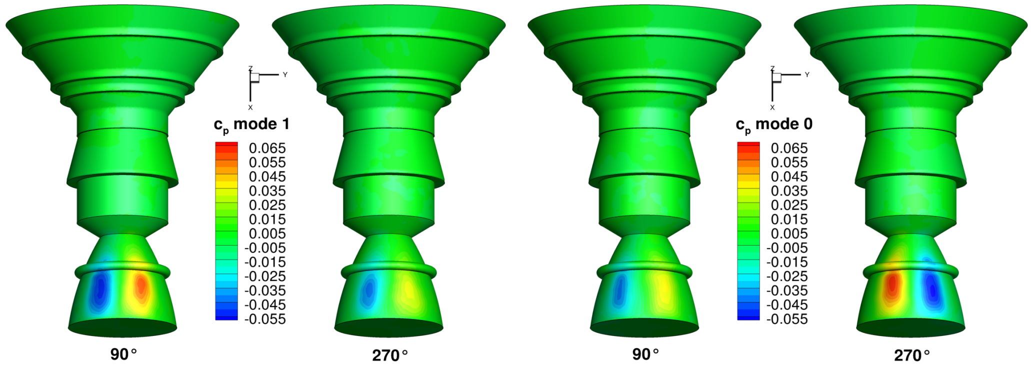

FIGURE 11. Surface c_p POD modes

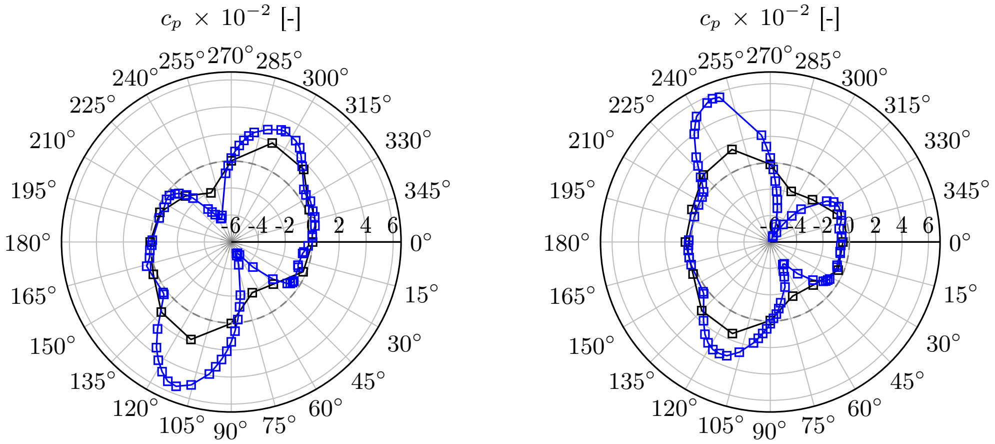

(a) Exp.: mode 0. CFD: mode 1.

(b) Exp.: mode 1. CFD: mode 0.

FIGURE 12. Surface c_p POD modes at location of ring 3. —□— Experimental data. —□— CFD data.

mode 0 the direction of surface pressure is symmetric with respect to the the booster plane, while it is antisymmetric for mode 1.

This becomes clearer when looking at the polar plots in Fig. 12, which compares the surface pressure POD data from the pressure transducers and the CFD results. The orientation of the angles is the same as Fig. 11 when looking in direction of flight. One notices that the order of the first two CFD modes is reversed and that the numerical results show significantly higher amplitude values. Even though these plots quantitatively do not agree well, the mode shapes are similar as they have the largest c_p amplitudes at similar angular locations.

The plot also shows the symmetry of the modes as described above. While Fig. 12(a) (experimental mode 0) is rotational symmetric with an angle of $180°$, Fig. 12(b) (experimental mode 1) is mirror symmetric with respect to the booster plane ($0°$ - $180°$).

4.5. *DMD of Velocity Data*

This section compares the DMD modes from experiment and simulation data for a sample length of $n = 256$. Additionally, the CFD data has been subsampled to $\mathrm{St}_S = 0.85$ to

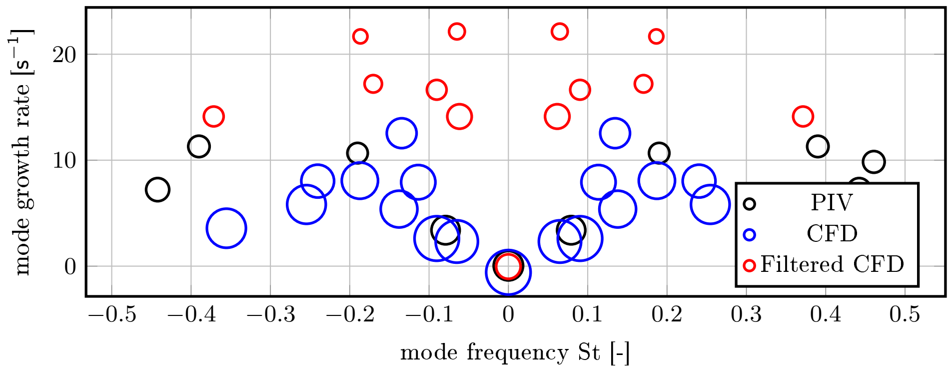

FIGURE 13. Damping plot for the most dominant DMD modes.

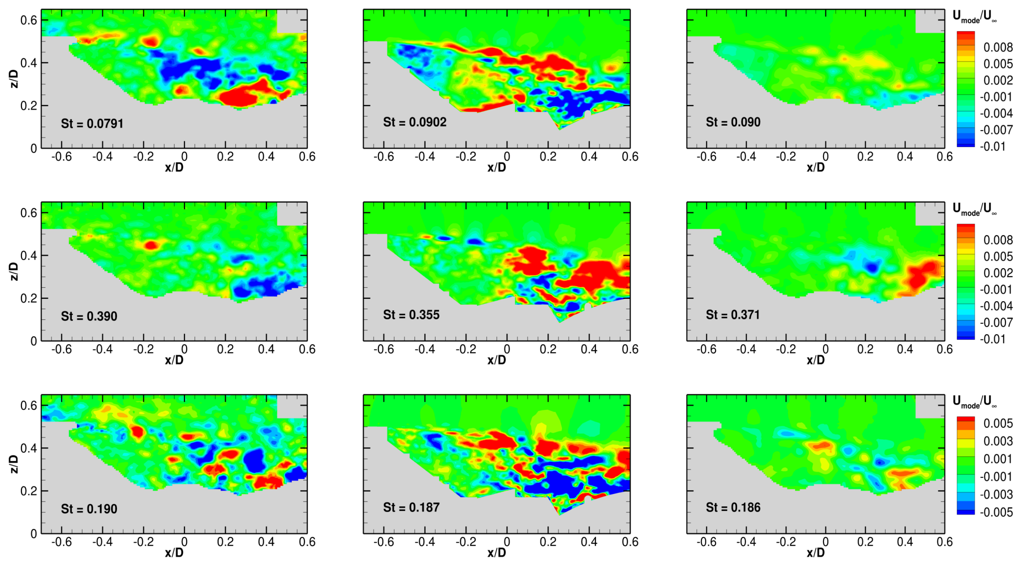

(a) PIV (b) CFD (c) Filtered CFD

FIGURE 14. Comparison of streamwise velocity DMD modes. All datasets have been sampled at similar sampling frequency and the same number of points.

match the experimental sampling frequency of $\mathrm{St}_S = 0.9$. Fig. 13 provides an overview of the most dominant modes. The damping plot shows the growth rate of different modes with respect to the mode frequency expressed in Strouhal number. In these type of plots the symbol size represents the relative mode amplitude. The figure shows that for all datasets modes are found around $\mathrm{St} = 0.09$, $\mathrm{St} = 0.37$ and $\mathrm{St} = 0.187$. Even though the datasets show similar dominant mode frequencies, the filtered CFD damping rates are much higher than for the other two datasets.

Fig. 14 shows the DMD mode shapes for the x-velocity component. All datasets have been sampled at a similar frequency. Also, the same number of samples has been used for the PIV and CFD datasets. A comparison of the mode shapes show that although the frequencies are very similar for most of the modes, the mode shapes differ greatly and that there is no coherent spatial shape visible as for the POD modes shown in

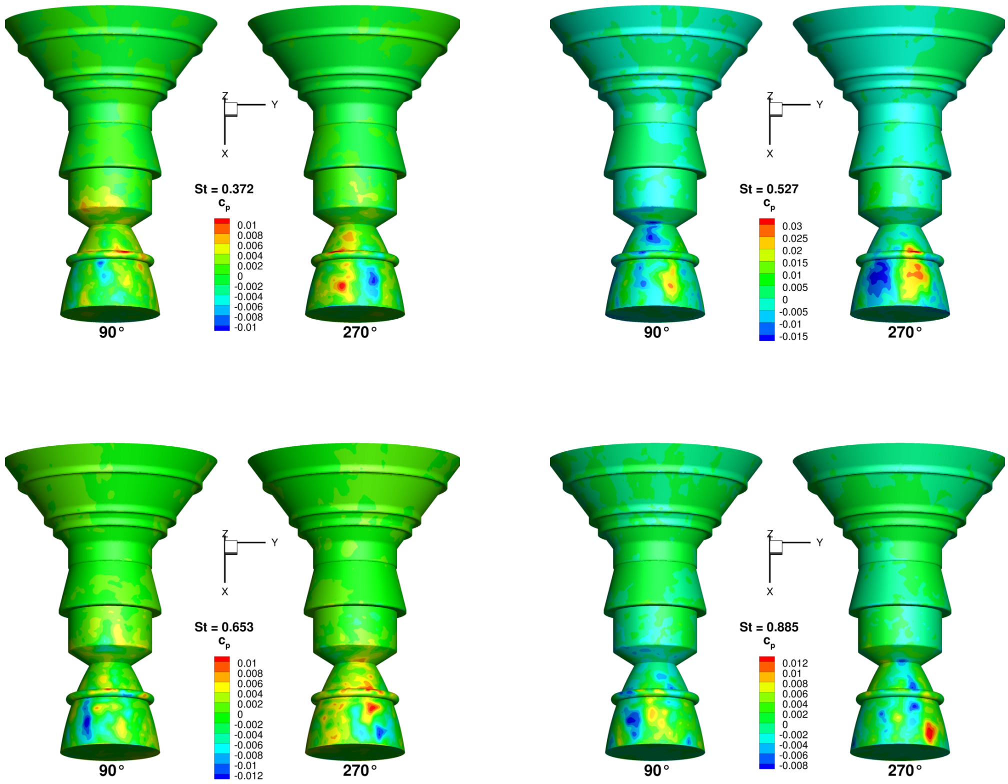

FIGURE 15. The four most dominant c_p dynamic modes.

Fig. 10. The sampling frequency and sample length have been varied systematically but there is no improvement towards more coherent spatial modes. One reason for this could be the presence of intermittent periodic structures that disappear and reappear during one sampling windows. This affects the DMD algorithm greatly because it is designed to identify non-vanishing periodical structures. We also investigated if the choice of the plane at $270°$ was rather unfortunate, because the surface pressure data (see e.g. Fig. 12) suggests that in this plane, very little fluctutations occur and that this might spoil the signal-to-noise ratio of the modes we are looking at. We therefore rotated the plane of investigation by $25°$ but the mode shapes did not improve.

Another possibility is that the modal structure of the flow field is inherently three-dimensional and that a reduction to 2D is not appropriate. This could only be answered by proper study of the full 3D CFD field dataset which is unfortunately out of the scope of the summer program. We must therefore conclude that although modes with similar frequencies are found for the experimental and numerical datasets, no clear mode shapes are visible and no direct comparison with the POD modes can be made.

4.6. *DMD of Pressure Data*

In order to get information on the main buffeting frequencies, we decomposed the 3D surface c_p distribution into its dynamic modes as shown in Fig. 15. This dataset has been sampled at a Strouhal number of $\mathrm{St}_S = 3.4$ using $n = 256$ samples giving a maximum resolvable frequency of $\mathrm{St}_{max} = 1.7$. The dynamic modes of c_p again show no clear mode shape except for $\mathrm{St}_S = 0.527$. This mode shows the same pattern as the experimental surface c_p distribution in Fig. 12(a) (CFD mode 1) although the mode's amplitude is about a factor of two smaller than the CFD POD mode. It must also be noted that the mode frequency of $\mathrm{St}_S = 0.527$ agrees very well with the strongest buffeting frequency reported in the literature [6].

5. Conclusion

In the present investigation the results from a high fidelity IDDES simulation were compared to high speed PIV measurements for a Mach 0.8 flow over the afterbody of the Ariane V launcher using straigtforward statistics (mean velocity and rms fluctuations), POD and DMD. Since PIV has a limited spatial resolution, it is not capable to capture all the flow length scales that are present. In order to asses this effect on the flow statisctics and the modal decompositions, the CFD data is spatially filtered in order to mimic the PIV measurement technique.

When comparing the time averaged flow fields, they look very similar in terms of flow topology and velocity magnitude. However there is a large difference in rms fluctuations, where the values predicted by CFD are much larger, even after filtering.

The results from POD applied to the velocity fields show an overall good agreement and the effect of spatial filtering is not very important. However a direct (one to one) comparison of the higher modes (larger than 3) is difficult because the energy spectrum is rather flat making the mode ranking very sensitive to the data ensemble size. Furthermore, it is found that the field of view that is considered has a non-negligible effect on the results (even the mode shapes) which is rather unexpected and needs more investigation.

Concerning the pressure POD modes a good overall agreement is found for the mode shapes, however the amplitude also greatly differs. This may be attributed to the fact that the temporal and spatial filtering involved with the pressure transducers was not taken into account when performing the CFD pressure POD.

The direct comparison of the DMD results shows dominant modes at similar frequencies for the experimental and the numerical datasets. However, coherent mode shapes could unfortunately not be extracted from these datasets. When comparing the surface c_p DMD results, a mode shape similar to the second largest POD mode could be extracted at a frequency close to the strongest base buffeting frequency as reported in the literature.

6. Acknowledgements

The authors gratefully acknowledge the SFB-TR40 for their support of this research activity during the Summer Program 2015. We also acknowledge the support from the ESA TRPs "Unsteady Subscale Force Measurements Within a Launch Vehicle Base Buffeting Environment" and "Launcher Base Flows and Shock Interaction Regions Improved Load Characterization".

References

[1] Berkooz, Gal and Holmes, Philip and Lumley, John L (1993) The proper orthogonal decomposition in the analysis of turbulent flows *Annual review of fluid mechanics*, **25(1)**, 539–575.

[2] Geurts, E.G.M. (2006) Steady and unsteady pressure measurements on the rear section of various configurations of the Ariane 5 launch vehicle. *National Aerospace Laboratory NLR, Report no. NLR-TP-2006-596*, Amsterdam, The Netherlands

[3] Grilli, Muzio and Schmid, Peter J and Hickel, Stefan and Adams, Nikolaus A (2012) Analysis of unsteady behaviour in shockwave turbulent boundary layer interaction. *Journal of Fluid Mechanics*, **700**, 16–28.

[4] Hannemann, K. and Luedeke, H. and Pallegoix, J. and Olliver, A. and Lambare, H. and Maseland, J. and Geurts, E. and Frey, M. and Deck, S. and Schrijer, F. and Scarano, F. and Schwane, R. (2011). Launch Vehicle Base Buffeting - Recent Experimental and Numerical Investigations. *Proc. of the 7th ESA Symposium on Aerothermodynamics for Space Vehicles*, Brugge, Belgium

[5] Jovanović, M. R. and Schmid, P. J. and Nichols, J. W. (2014). Sparsity-promoting dynamic mode decomposition. *Physics of Fluids*, **26**

[6] Ludeke, H., Mulot, J.D. and Hannemann, K Launch Vehicle Base Flow Analysis Using Improved Delayed Detached-Eddy Simulation. *AIAA Journal*, **53** (9), 2454–71.

[7] Lumley, J.J. (1970). Stochastic Tools in Turbulence. *Academic Press*.

[8] Muld, Tomas W and Efraimsson, Gunilla and Henningson, Dan S (2012) Flow structures around a high-speed train extracted using proper orthogonal decomposition and dynamic mode decomposition. *Computers & Fluids*, **57**, 87–97.

[9] Sirovich, Lawrence (1987) Turbulence and the dynamics of coherent structures. *Quarterly of applied mathematics*, **45**, 561–571.

[10] Schmid, Peter J (2010). Dynamic mode decomposition of numerical and experimental data. *Journal of Fluid Mechanics*, **656**, 5–28.

[11] Schrijer, F. and Sciacchitano, A. and Scarano, F. and Hannemann, K. and Pallegoix, J. and Maseland, J. and Schwane, R. (2011). Experimental Investigation of Base Flow Buffeting on the Ariane 5 Launcher Using High Speed PIV. *Proceedings of the 7th European Symposium on Aerothermodynamics for Space Vehicles*, Brugge, Belgium.

[12] Schmid, PJ and Li, L and Juniper, MP and Pust, O (2011) Applications of the dynamic mode decomposition. *Theoretical and Computational Fluid Dynamics*, **25 (1-4)**, 249–259.

[13] Schmid, Peter J (2011). Application of the dynamic mode decomposition to experimental data. *Experiments in fluids*, **50 (4)**, 1123–1130.

[14] Schmid, Peter J and Violato, Daniele and Scarano, Fulvio (2012). Decomposition of time-resolved tomographic PIV. *Experiments in fluids*, **52(6)**, 1567–1579.

[15] Tu, J. H. and Rowley, C.W. and Luchtenburg, D.M. and Brunton, S.L. and Kutz, J.N. (2013) On Dynamic Mode Decomposition: Theory and Applications. *ArXiv e-prints*, Provided by the SAO/NASA Astrophysics Data System (http://adsabs.harvard.edu/abs/2013arXiv1312.0041T)

[16] Schwamborn, D. and Gerhold, T. and Heinrich, R. (2006) The DLR-TAU-Code: Recent Applications in Research and Industry. *European Conference on*

Computational Fluid Dynamics, ECCOMAS CFD.

[17] STATNIKOV, V. AND SAYADI, T. AND MEINKE, M . AND SCHROEDER, W. AND SCHMID, P. (2013). Dynamic Mode Decomposition of Supersonic and Transonic Wakes of Generic Space Launcher Configurations. *Proc. of the Summer Program 2013*.